



Multi-messenger Model for the Prompt Emission from GRB 221009A

Annika Rudolph^{1,2} , Maria Petropoulou^{3,4} , Walter Winter² , and Željka Bošnjak⁵ ¹ Niels Bohr International Academy and DARK, Niels Bohr Institute, University of Copenhagen, Blegdamsvej 17, D-2100, Copenhagen, Denmark
annika.lena.rudolph@nbi.ku.dk² Deutsches Elektronen-Synchrotron DESY, Platanenallee 6, 15738 Zeuthen, Germany³ Department of Physics, National and Kapodistrian University of Athens, University Campus Zografos, GR 15783, Athens, Greece⁴ Institute of Accelerating Systems & Applications, University Campus Zografos, GR 15783, Athens, Greece⁵ Faculty of Electrical Engineering and Computing, University of Zagreb, Unska ul. 3, 10000 Zagreb, Croatia

Received 2022 December 6; revised 2023 January 27; accepted 2023 January 27; published 2023 February 16

Abstract

We present a multi-messenger model for the prompt emission from GRB 221009A within the internal shock scenario. We consider the time-dependent evolution of the outflow with its impact on the observed light curve from multiple collisions, as well as the self-consistent generation of the electromagnetic spectrum in synchrotron and inverse Compton-dominated scenarios. Our lepto-hadronic model includes UHE protons potentially accelerated in the outflow, and their feedback on spectral energy distribution and on the neutrino emission. We find that we can roughly reproduce the observed light curves with an engine with varying ejection velocity of ultrarelativistic material, which has an intermediate quiescent period of about 200 s and a variability timescale of ~ 1 s. We consider baryonic loadings of 3 and 30 that are compatible with the hypothesis that the highest-energetic LHAASO photons might come from UHECR interactions with the extragalactic background light, and the paradigm that energetic GRBs may power the UHECR flux. For these values and the high dissipation radii considered, we find consistency with the nonobservation of neutrinos and no significant signatures on the electromagnetic spectrum. Inverse Compton-dominated scenarios from the prompt emission are demonstrated to lead to about an order of magnitude higher fluxes in the HE range; this enhancement is testable via its spectral impact in the Fermi-GBM and LAT ranges.

Unified Astronomy Thesaurus concepts: [Cosmic rays \(329\)](#); [Cosmological neutrinos \(338\)](#); [High-energy astrophysics \(739\)](#); [Nonthermal radiation sources \(1119\)](#); [Gamma-ray bursts \(629\)](#)

1. Introduction

Gamma-ray bursts (GRBs) are extremely energetic explosions involving the collapse of a massive star or the merger of two compact objects. As their name suggests, GRBs release most of their electromagnetic output in γ -rays within a short period of time (ranging from tens of milliseconds to hundreds of seconds). This brief and variable emission, known as the prompt GRB phase, is followed by the afterglow, a long-lasting multiwavelength emission (for a review, see, e.g., Kumar & Zhang 2015). The prompt emission is thought to be produced in a relativistic collimated plasma outflow (jet) launched by the central engine via some dissipative mechanism. For kinetically dominated jets, a leading scenario involves energy dissipation and particle acceleration at internal shocks that are produced when portions of the jet are moving outward with varying Lorentz factors (e.g., Kobayashi et al. 1997; Daigne & Mochkovitch 1998). Part of the remaining jet energy can be later transformed to nonthermal radiation at a relativistic blast wave sweeping up material from the circumburst medium and powering the afterglow (Rees & Meszaros 1992; Chiang & Dermer 1999).

GRBs are one of the prime targets of multi-messenger astronomy, as they have been detected in gravitational waves (GW170817/GRB 170817, Abbott et al. 2017) and have been proposed as candidate sources of ultra-high-energy cosmic rays

(UHECRs) and astrophysical neutrinos (e.g., Vietri 1995; Waxman 1995). While the contribution of typical luminosity GRBs during their prompt phase to the diffuse neutrino flux measured by IceCube has been constrained to $\lesssim 1\%$ of the diffuse astrophysical neutrino flux (Abbasi et al. 2022), the hypothesis that GRBs are UHECR sources cannot be ruled out yet (for a recent review, see Kimura 2022). In fact, GRBs populating the high end of the isotropic γ -ray energy distribution ($E_{\gamma, \text{iso}} > 10^{54}$ erg) may provide the necessary energy output per event for powering UHECRs, requiring only a moderate baryonic loading (defined as the energy injected into nonthermal protons versus electrons) and without violating existing neutrino limits (Rudolph et al. 2022). In addition, energetic bursts may be detected as a single source (e.g., Gao et al. 2013).

On 2022 October 9th, a very bright GRB was observed at redshift $z = 0.151$ (de Ugarte Postigo et al. 2022). The burst triggered the Gamma-Ray Burst Monitor (GBM) on board Fermi at 2022 October 09 13:16:59.000 UT (Veres et al. 2022), about an hour before the detection of a hard X-ray transient by the Burst Alert Telescope (BAT) of the Neil Gehrels Swift satellite (Dichiara et al. 2022; Lesage et al. 2022). The prompt phase of GRB 221009A consisted of a precursor (at about 10 s), followed by an extremely bright emission period about 200 s post GBM trigger. Overall, the prompt emission period lasted roughly 327 s and was composed of several peaks (Lesage et al. 2022). The preliminary Konus-Wind light curve showed several peaks of roughly 40 s duration (Frederiks et al. 2022); the initial peaks were separated from the late-time peak by a quiescent period of about 220 s. Some short-timescale variability on the order of seconds might be also visible in the

Table 1
Fireball Characteristics and Microphysics Parameters for the Different Scenarios

Quantity	Symbol	“ R_{16} ” scenario		“ R_{17} ” scenario	
		SYN-dom.	IC-dom.	SYN-dom.	IC-dom.
Engine time for main emission period	t_{main} [s]		74		
Engine quiescent time	t_{quiet} [s]		213		
Engine time for late-time activity	t_{late} [s]		8		
Variability timescale of engine activity	δt_{var} [s]		1.4		
Averaged Γ at beginning	$\langle \Gamma_{\text{ini}} \rangle$		265		663
Averaged Γ at end	$\langle \Gamma_{\text{fin}} \rangle$		228		570
Averaged Γ of emitting plasma	$\langle \Gamma_{\text{em}} \rangle$		293		731
Averaged radius of emitting plasma	$\langle R_{\text{Coll}} \rangle$ [cm]		1.2×10^{16}		2.0×10^{17}
Total energy transferred to nonthermal electrons	$E_{\text{e,NT}}$ [erg]	4.6×10^{54}	9.3×10^{54}	4.8×10^{54}	9.3×10^{54}
Initial fireball kinetic energy	$E_{\text{kin,ini}}$ [erg]	5.7×10^{56}	9.2×10^{56}	3.8×10^{57}	7.1×10^{57}
Averaged maximal proton energy	$\langle E_{\text{p,max}} \rangle$ [10^{11} GeV]	21.9	2.7	23.7	1.1
Emitted gamma-ray energy ($1\text{--}10^4$ keV)	$E_{\gamma,\text{iso}}$ [erg]	2.9×10^{54}	3.1×10^{54}	2.9×10^{54}	2.9×10^{54}
Relative fraction of energy transferred to magnetic field	$f_{\text{B}/\text{e}} = \epsilon_{\text{B}}/\epsilon_{\text{e}}$	1	10^{-3}	1	10^{-3}
Relative fraction of energy transferred to acc. protons	$f_{\text{p}/\text{e}} = \epsilon_{\text{p}}/\epsilon_{\text{e}}$	3	3	30	30
Power-law index of accelerated electrons	p_{e}			2.2	
Minimum Lorentz factor of accelerated electrons	$\gamma'_{\text{e,min}}$ [10^4]	3	9	6	11
Power-law index of accelerated protons	p_{p}			2.0	
Minimum Lorentz factor of accelerated electrons	$\gamma'_{\text{p,min}}$			10	

Note. All listed energies refer to the isotropic equivalent values. Energies and times are reported in the source (engine) frame. Averaged quantities are computed weighing with the shell mass ($\langle \Gamma_{\text{ini}} \rangle$ and $\langle \Gamma_{\text{fin}} \rangle$) or with the dissipated energy of a collision ($\langle \Gamma_{\text{em}} \rangle$, $\langle R_{\text{Coll}} \rangle$, and $\langle E_{\text{p,max}} \rangle$). The maximal proton energies are computed considering synchrotron and adiabatic losses and equally refer to the engine frame.

0.4–100 MeV AGILE MCAL light curve (Ursi et al. 2022) and INTEGRAL SPI-ACS light curve.⁶ The burst was also observed in high energies (HE, $\gtrsim 0.1$ GeV) by the Fermi Large Area Telescope (LAT), starting about 200 s after the GBM trigger (i.e., during the prompt phase) and extending up to ~ 25 ks into the afterglow phase (Pillera et al. 2022). In addition, very high-energy (VHE, > 100 GeV) photons were detected by LHAASO, but their association to the prompt phase is not clear, given that these photons were observed within a period of up to 2000 s after trigger (Yong Huang et al. 2022). It has been speculated that the highest-energy photons (up to 18 TeV) might come from UHECR interactions with the extragalactic background light (EBL), because such energetic photons escaping the source would be otherwise attenuated by the EBL (Alves Batista 2022; Das & Razzaque 2022; Mirabal 2022). These scenarios require a significant amount of energy carried by UHE protons, which might also leave signatures in the electromagnetic spectrum.

The extreme brightness of this burst caused pileup in almost all GRB detectors, namely Fermi-GBM and LAT, Konus-Wind, and AGILE. For this reason, detailed spectral analysis was unavailable at the time of writing. Preliminary analysis of LAT data (100 MeV–1 GeV) for 200–800 s after the GBM trigger provided an estimate of the photon index (-1.87 ± 0.04) and the photon flux ($(6.2 \pm 0.4) \times 10^{-3}$ ph $\text{cm}^{-2} \text{s}^{-1}$) (Pillera et al. 2022), but the time interval excluded from the analysis was recently extended to 300 s (Omodei et al. 2022). Hence, the relevance of these results to the main GRB episode detected by GBM is not yet clear. Moreover, preliminary analysis of Konus data during the brightest phase of the event (i.e., $\sim 180\text{--}200$ s after the Konus trigger) produced a rest-frame peak energy of $E_{\text{peak}} = 1150$ keV and

$E_{\gamma,\text{iso}} \simeq 3 \times 10^{54}$ erg. No associated muon-neutrino track was detected by IceCube in a time range of $[-1 \text{ hr}, +2 \text{ hr}]$ from the initial GBM trigger, which resulted in an upper limit on the muon-neutrino fluence of 3.9×10^{-2} GeV cm^{-2} assuming an E^{-2} neutrino spectrum (The IceCube Collaboration 2022). The inferred γ -ray isotropic energy, the proximity of this event to Earth, and the lack of prompt neutrino detection make GRB 221009A a unique case for the study of multi-messenger signatures from GRBs.

In this letter, we present a multi-messenger model for the prompt emission of GRB 221009A. Under the assumption that protons and electrons are accelerated at the fastest possible rate in internal shocks occurring at different radii within the jet, we compute the multi-messenger emission from each collision while taking into account the varying physical conditions in the outflow and the UHECR feedback on both the photon and neutrino emissions. Our goal is to test the hypothesis of UHECR acceleration in the GRB jet by comparing the self-consistently computed broadband photon spectrum and the accompanying neutrino flux with available observational information. Because details on the prompt spectrum are not yet available and the mentioned pileup effects likely introduce some degeneracy, our model also has some predictive power. In this work, we indicatively use the following observables: (1) the rest-frame peak energy $E_{\text{peak}} = 1150$ keV (as fitted for the onset of the bright emission period by Konus), (2) the estimated fluence in the GBM band $\mathcal{F}_{\text{GBM}} = 2.91 \cdot 10^{-2}$ erg cm^{-2} (1–1000 keV) and (3) the approximate light curve structure observed by Konus and INTEGRAL SPI-ACS. Peak energy and fluence are reproduced within $\pm 5\%$.

2. Model and Implementation

Our model is fully described in an accompanying paper (Rudolph et al. 2022), to which we refer the interested readers

⁶ https://grbalpha.konkoly.hu/static/share/GRB221009A_GCN_GRBAlpha.pdf

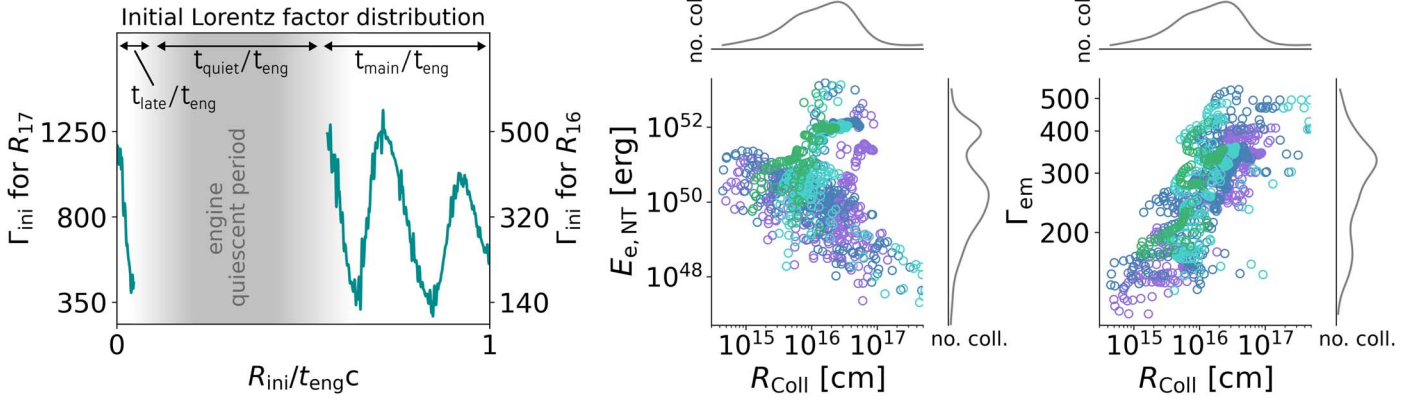


Figure 1. Left: Distribution of Lorentz factors of plasma shells launched by the central engine. Here, R_{ini} is the initial radius of a plasma shell. Two cases are shown, respectively leading to high (left axis) and low (right axis) collision radii. The parameter t_{eng} represents the total activity time of the engine, i.e., $t_{\text{eng}} = t_{\text{main}} + t_{\text{quiet}} + t_{\text{late}}$. Middle and right: Two-dimensional phase space of the collision radius and the total energy carried by nonthermal electrons (middle) or the Lorentz factor of the emitting plasma (right). Results are shown for the case of low dissipation radii and SYN-dominated electron cooling (Table 1). The collisions (each represented by a circle) are distinguished by color according to the time interval during which they will be observed: purple (0–36.5 s), blue (36.5–71.5 s), aquamarine (71.5–129.5 s), and green (from 308.5 s). Grouped collisions correspond to four distinctive pulses of the light curve shown in Figure 2.

for details. Here, we summarize the key points of the model and present its main parameters in Table 1. In short, a relativistic outflow is discretized as shells ejected with different Lorentz factors from a central engine operating over a time t_{eng} (as measured in the engine rest frame). Shells catch up with each other and merge at a radius R_{Coll} from the central emitter, where energy is dissipated and particles are accelerated. Shells continue to propagate, merge, and dissipate energy until their velocity distribution is such that no more collisions occur. The energy dissipated in each inelastic collision, which can be obtained from energy and momentum conservation, is distributed into nonthermal electrons, protons, and magnetic fields (for simplicity, we assume that no energy remains in thermal plasma). We introduce the partition parameters $f_{p/e}$ (baryonic loading) and $f_{B/e}$ (magnetic loading) describing the ratio between proton/electron and magnetic/electron energy density, respectively (here only referring to accelerated, nonthermal particles). Assuming that the sub-MeV prompt spectrum is predominantly produced by synchrotron radiation of accelerated electrons, we normalize the fireball kinetic energy to the total energy transferred to nonthermal electrons $E_{e, \text{NT}}^{\text{tot}}$ that is needed to produce a given $E_{\gamma, \text{iso}}$. Based on our simulations, the energy dissipation efficiency⁷ of the fireball is $\varepsilon_{\text{diss}} \simeq 0.04$, for the specific Lorentz factor distribution assumed here. The required fireball kinetic energy (isotropic equivalent) is then indirectly related to the energy partition parameters, and in particular, it increases with increasing baryonic loading as $E_{\text{kin, ini}} = \varepsilon_{\text{diss}}^{-1} E_{e, \text{NT}}^{\text{tot}} (1 + f_{p/e} + f_{B/e})$. In contrast to Rudolph et al. (2022), we normalize all models to a similar $E_{\gamma, \text{iso}}$, leading to higher $E_{\text{kin, ini}}$ for cases with a low electron synchrotron efficiency.

To reproduce the structure of the observed light curve, here we use a varying Lorentz factor profile (see Figure 1, left panel), without addressing the question of which engine properties would lead to such a profile. The initial Lorentz factor distribution is obtained in two steps: First, we reproduce the broad structure of the observed light curve (a dip and two bright peaks, followed by a quiescent period and late-time

emission) through sine waves with relative amplitudes matching the observed flux variations and durations of these engine activity intervals. The engine activity is correspondingly characterized by three time intervals: the activity time of the main emission period t_{main} , the engine quiescent time t_{quiet} , and the activity time for the late-time emission t_{late} . Second, after inferring a short-time variability timescale of $\delta t_{\text{var}} \simeq 1$ s from observations, we add modulations on this timescale, with amplitude drawn randomly from a normal distribution with standard deviation $0.08 \cdot \langle \Gamma \rangle$. From 20 realizations of this random process, we select the initial configuration that best matches the observed light curve by eye.

We present two different scenarios for the initial Lorentz factor distribution—denoted as “ R_{16} ” and “ R_{17} ”—that produce collisions at an average radius $\langle R_{\text{Coll}} \rangle \sim 10^{16}$ cm and $\langle R_{\text{Coll}} \rangle \sim 2 \times 10^{17}$ cm, respectively, and probe higher and lower typical plasma densities. We verified that, in both scenarios, the bulk of energy dissipation occurs below the estimated deceleration radius for typical parameters of the circumburst medium. These scenarios are motivated by estimates for the optical thickness of the emitting plasma to $\gamma\gamma$ pair production (Murase et al. 2022) and the requirement that the bulk of energy is dissipated below the approximate deceleration radius. In principle, high Γ factors are also expected from the empirical $E_{\gamma, \text{iso}} - \Gamma$ relationships (Ghirlanda et al. 2018). As an example, we show for “ R_{16} ” the two-dimensional distributions of the nonthermal electron energy and the Lorentz factor of the emitting shell with collision radius in the middle and right panels of Figure 1.

We self-consistently evaluate the emission from nonthermal electrons and protons, accelerated in shocks from the collision of shells, and injected with power-law distributions into the radiation zone, which is the hot plasma of the merged shell. The full-burst emission is then integrated over all collisions, taking into account the curvature of the emitting surface. The maximal electron and proton energies are limited by the dominating energy-loss processes, assuming efficient acceleration (operating at the Bohm limit). For each scenario, the minimum electron Lorentz factor $\gamma'_{e, \text{min}}$ is set such that the peak energy of 1060 keV is reproduced; the minimal proton energies are generally fixed to $\gamma'_{p, \text{min}} = 10$. We assume a power-law slope of primary protons of $p_p = 2.0$ as in

⁷ The fireball radiative efficiency is then found by multiplying $\varepsilon_{\text{diss}}$ with the fraction of energy carried by primary electrons and the synchrotron radiative efficiency.

Rudolph et al. (2022). In our model, the primary electron power-law slope would usually be determined by the high-energy photon index. As there was no reliable measurement for the high-energy slope at the time of writing, we adapt $p_e = 2.2$ as suggested for mildly relativistic shocks (Crumley et al. 2019). We then numerically solve⁸ the coupled system of integrodifferential equations describing the temporal evolution of particle distributions (electrons/positrons, photons, protons, neutrons, pions, muons, neutrinos) including the relevant processes, such as synchrotron emission and absorption, inverse Compton scattering (ICS), photopair and photopion production, $\gamma\gamma$ pair production, adiabatic cooling, and escape. Our approach fully captures the electromagnetic cascade induced by photohadronic and $\gamma\gamma$ pair production in each merged shell.⁹

As discussed in detail in Rudolph et al. (2022), the electromagnetic spectrum will be, even in the lepto-hadronic case, dominated by the primary leptonic emission: a synchrotron component peaking in the MeV band and an inverse Compton component emerging at higher energies (GeV band) for low enough $f_{B/e}$ values. We therefore discuss two scenarios, a synchrotron (“SYN”)–dominated one and an inverse Compton (“IC”)–dominated one, each with different values of $f_{B/e}$ (see Table 1), characterized by different photon spectra and light curves. We also include the effects of EBL attenuation using the model of Dominguez et al. (2011), calculated with the open-source GAMMAPY package (Deil et al. 2018; Nigro et al. 2019).

A crucial parameter in every multi-messenger model is the baryonic loading. Rudolph et al. (2022) showed that $f_{p/e} \gtrsim 3$ is required for $E_{\gamma, \text{iso}} \simeq 3 \times 10^{54}$ erg, if such energetic GRBs ought to power the UHECRs. Much higher baryonic loadings in combination with low R_{Coll} lead to spectral distortions of the photon spectrum (even in the GBM and LAT bands), and efficient neutrino production, which might be in tension with multi-messenger limits (for details, see Section 6 in Rudolph et al. 2022). A different argument comes from the observed VHE photons in LHAASO, if these were produced by interactions of UHECRs with the EBL (Alves Batista 2022; Das & Razzaque 2022; Mirabal 2022). Das & Razzaque (2022) derive an isotropic-equivalent $E_{p, \text{iso}} \simeq 3.9 \times 10^{54}$ erg for escaping cosmic rays in the range 0.1–100 EeV, which yields $E_{p, \text{iso}} \gtrsim 2 \times 10^{55}$ erg bolometrically corrected for our considered energy range, if all UHECRs free-streamingly escape. In our model, this energy budget is met for $f_{p/e} \gtrsim 3$. For Alves Batista (2022), the given fraction into UHECRs is lower, but the bolometric correction factor is much higher, as only UHECRs at the highest energies were considered in that work. In what follows, we choose $f_{p/e} = 3$ for “ R_{16} ” and $f_{p/e} = 30$ for “ R_{17} .” The former is compatible with the above estimates, while the latter is a more aggressive version (still compatible with neutrino bounds) that will challenge the GRB energetics in terms of the kinetic energy required. Purely leptonic results will not be shown, as we found no substantial modifications due to hadronic contributions in the observable photon spectra for the baryonic loadings considered.

3. Results

Light curves. By construction of our model, the rough structure of the light curves shown in Figure 2 reflects the initial Lorentz factor distribution in Figure 1. Each pulse of the synthetic light curves is formed by shells colliding over a wide range of radii (as can be inferred from the color coding in Figure 1). Collisions within the same pulse may thus have different opacities, potentially introducing time lags between different energy ranges.

In the left panel, we indicate the observed light curves of INTEGRAL SPI-ACS and Konus, shifted to match the beginning of our synthetic light curve that does not include the precursor emission. The general structure of the observed light curve is reproduced by our model, but our results should also be representative for light curves with a similar general structure. The relative intensity of the two bright pulses in the observed light curve may be strongly impacted by pileup effects in the detector. Here, we assumed that the first bright peak is intrinsically much more energetic than the second one. In our model the relative height of the peak is controlled by the ratio of Lorentz factors of the colliding shells (e.g., a bright peak is produced when this ratio is large). The γ -ray light curves available at the time of writing indicate short-time variability on the second timescale, which was modeled by stochastic variations of Γ_{ini} on a timescale $\delta t_{\text{var}} = 1.4$ s (see Figure 1). However, if refined analysis of the light curves revealed variability on a shorter timescale, this would shift the typical collision radius inwards where the densities are higher. As shown in Rudolph et al. (2022), this would lead to stronger signatures of secondary particles, such as secondary leptons and neutrinos, for the same baryonic loading.

The synthetic HE light curve (shown in the middle panel of Figure 2) is very similar to the keV–MeV light curve. Preliminary analysis of LAT data using GTBURST¹⁰ showed no evidence for a fourth peak in the 20 MeV–300 GeV light curve. If this is later verified by detailed LAT analysis, then late-time collisions with low Lorentz factors will be needed in our model in order to suppress the late-time HE emission due to high internal opacity to $\gamma\gamma$ pair production. While the shape of the HE light curve is similar in the SYN- and IC-dominated scenarios, the HE flux is higher in the latter case, suggesting that primary electrons are cooling more efficiently via ICS (see also next paragraph). Non-negligible VHE emission between 1 and 10 TeV is also expected in the IC-dominated scenario (right-hand panel), with a light curve similar to that of the lower-energy bands.

Photon spectra. Figure 3 shows the predicted time-integrated photon fluences as a function of observed energy; the inset is a zoom-in on the spectra around the peak, including the photon index (which is defined as the spectral slope of $dN_{\text{ph}}/dE_{\text{obs}}$).

We first discuss the results for the SYN-dominated cases (blue lines in both panels). The spectrum around the peak is by construction independent of the typical collision radius, and it is given by the standard synchrotron fast-cooling predictions: approaching a photon index $-3/2$ below the peak and $-(p_e + 2)/2$ above the peak. Differences between “ R_{17} ” and “ R_{16} ” are visible at low and high energies with respect to the MeV peak. For “ R_{16} ,” where the densities are higher, emission of secondaries increases the fluence in the eV range, leading to a low-energy spectral break. However, the spectrum in the LAT

⁸ The simulations are performed with the proprietary code AM³ (Gao et al. 2017).

⁹ We do not consider interactions of particle populations between shells.

¹⁰ <https://fermi.gsfc.nasa.gov/ssc/data/analysis/scitools/gtburst.html>

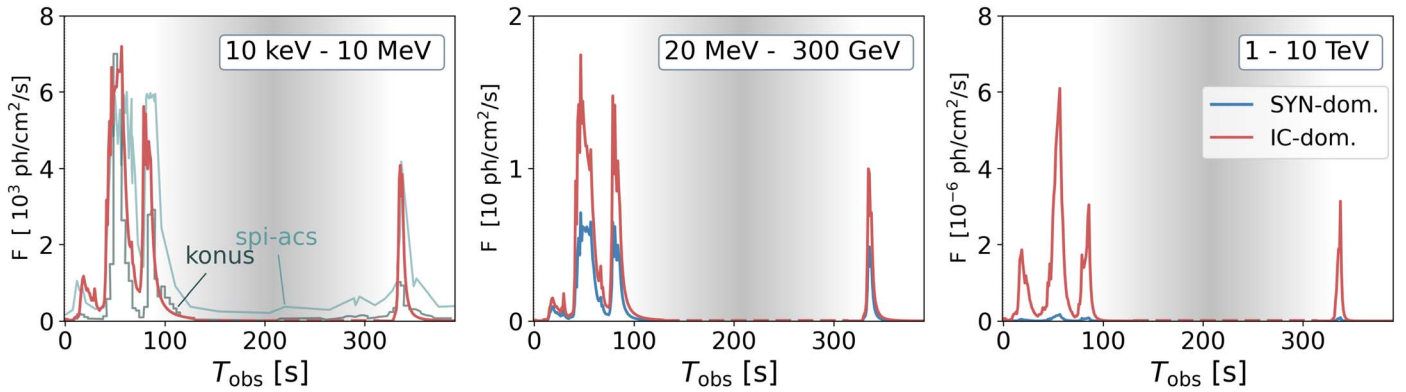


Figure 2. Synthetic light curves for three energy ranges obtained in the “ R_{16} ” scenario for the IC- and SYN-dominated cases (in all panels indicated as red and blue curves, respectively; see legend in right panel). In the left panel, we show only the IC-dominated case, as it resembles the SYN-dominated one. We also add observed light curves of Konus and INTEGRAL SPI-ACS that operate in a comparable energy range, renormalized to match the same scale and shifted in time to match the same peak times (-175 s for Konus, and -225 s for INTEGRAL SPI-ACS). We set $T_{\text{obs}} = 0$ for the synthetic light curve as the minimum collision time in the observer’s frame.

band is still dominated by the synchrotron emission of fast-cooling primaries. For “ R_{17} ,” the power-law spectrum with photon index -1.5 extends to the lowest energies (until synchrotron self-absorption becomes important), while higher maximal synchrotron energies yield a harder high-energy spectrum.

In the “ R_{16} ” IC-dominated case (red curves in left panel), the spectral slope below the peak is still -1.5 , but the HE emission (in the LAT range) is modified by the ICS emission of primary and secondary leptons that creates an almost flat spectrum (i.e., photon index ~ -2). In this case, the peak of the broadband spectrum is shifted to ~ 1 GeV. In the “ R_{17} ” IC-dominated case (red curves in right panel), the photon index below the MeV peak (but not within the GBM band) becomes asymptotically ~ -1.25 , which is the highest value that can be produced in our model. This is indicative of electron cooling via ICS in the Klein–Nishina regime (Daigne et al. 2011). In the LAT band, the spectrum is a power law that extends to about 10 TeV (where the Klein–Nishina ICS emission of primary electrons with Lorentz factor $\gamma'_{e,\text{min}}$ dominates). However, due to EBL attenuation, this spectral feature is washed out. We note that, in the “ R_{17} ” IC-dominated case, the contribution of secondary leptons in the GBM and LAT bands is negligible. For a more detailed discussion on spectra and their decomposition, we point to Sections 4 and 5 in Rudolph et al. (2022).

In addition to the full time-integrated spectra, we computed the spectra for the three main emission periods, namely the first two bright pulses and the late-time pulse (not explicitly shown). Finding little difference in the spectra for these three pulses, we predict no significant spectral evolution during these three emission periods.

Neutrinos. We include in Figure 3 the predicted neutrino spectra (per flavor)¹¹ and the corresponding IceCube limits (The IceCube Collaboration 2022) for the different scenarios as dashed curves. We also compute the number of expected neutrino events in IceCube with the appropriate point-source effective area for the decl. range 18° – 21° (Abbasi et al. 2021), and find $n_{\nu_\mu} = 0.012$ (0.006) for the “ R_{17} ” SYN- (IC-) dominated case and $n_{\nu_\mu} = 0.17$ (0.29) for the “ R_{16} ” SYN- (IC-) dominated case. The predicted neutrino fluences are thus below the IceCube limits in all cases and are consistent with

nondetection, as a result of the relatively large R_{Coll} paired with the chosen baryonic loadings, in consistency with the findings in one-zone models (Ai & Gao 2022; Murase et al. 2022). For “ R_{16} ,” however, a baryonic loading of $f_{p/e} \gg 3$ is expected to be in tension with neutrino limits, and if observations eventually favor a variability timescale $\delta t_{\text{var}} \lesssim 1$ s, the baryonic loading would be limited to an even smaller value.

Contrary to Rudolph et al. (2022), we normalize the initial engine kinetic energy to achieve the same γ -ray isotropic energy, which for the IC-dominated scenarios increases the required energy (see Table 1). This increases the energy transferred to nonthermal protons and subsequently the neutrino fluences. The effect can be noticed clearly for the “ R_{16} ” scenario. For the “ R_{17} ” scenario, the neutrino production efficiency is limited by the low(er) maximal proton energies, due to the lower magnetic fields obtained in the IC-dominated case. It is interesting that the peak neutrino energies of 10^{17} – 10^{19} eV exceed the expectation of the standard neutrino model for GRBs (10^{15} eV; see, e.g., Hummer et al. 2012) by at least two orders of magnitude in energy. This is a result of the synchrotron-cooling-dominated spectral indices below the peak (the photon number density peaks at lower energies) paired with weak magnetic field effects on the secondaries as a consequence of large R_{Coll} . Therefore, energetic GRBs may be a target for future radio detection experiments.

4. Discussion

There are a number of effects that can be included in order to enrich model. For example, the different pulses may be produced by collisions of shells with very different Lorentz factor ranges or even microphysics parameters. This can cause a combination of SYN- and IC-dominated scenarios in different peaks (see also Zhang et al. 2022, for the reverse shock), or suppression of VHE emission in others (by low Lorentz factors enhancing the $\gamma\gamma$ optical thickness and also the neutrino production). One may speculate that a nonobservation of the late-term peak by Fermi-LAT or a contribution to the LHAASO signal could be produced by such effects. Within each peak, low Lorentz factors and a strong correlation between collision radius and observation time can cause an early suppression of VHE photons, which may be interpreted as a delay (Bustamante et al. 2017). While our spectral index above the peak can be adjusted by the electron injection index

¹¹ The synchrotron cooling of pions and muons is taken into account; for a more detailed discussion, see Rudolph et al. (2022).

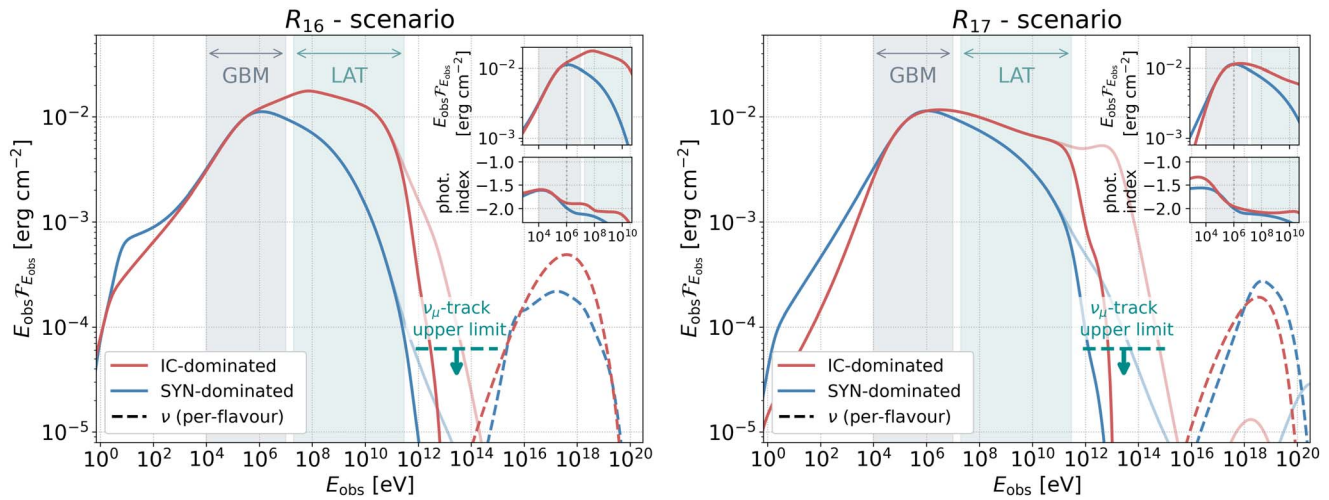


Figure 3. Modeled spectra $E_{\text{obs}} \mathcal{F}_{E_{\text{obs}}}$ for the (left) “ R_{16} ” and “ R_{17} ” (right) scenarios, in both cases, including a SYN- and an IC-dominated scenario (for parameters, see Table 1). Transparent curves correspond to the fluence without taking EBL attenuation into account, and dashed curves to the per-flavor neutrino fluences. The latter are compared with the IceCube upper limit reported in The IceCube Collaboration (2022). The inset shows a zoom-in to the spectrum around the peak in the Fermi-GBM/LAT range (indicated as a shaded region in all plots), with a dotted vertical line at 1060 keV to indicate the position of the observed peak. In the inset we further indicate the photon indices, that are defined of the slope of $dN_{\text{ph}}/dE_{\text{obs}}$.

and the efficiency of ICS, our model may not accommodate very hard low-energy photon indices of ~ -1 , unless additional components, such as photospheric thermal emission, are considered. In lepto-hadronic models these components would increase the number of target photons available for photo-hadronic interactions. We note that the highest photon index of -1.25 was obtained in the “ R_{17} ” IC-dominated scenario, but well below the GBM band. Whether such a high dissipation radius is indeed realistic should be confirmed by observations of the variability timescale and estimates of the Lorentz factor.

The GRB central engine may be a newly formed accreting black hole or magnetar. For energetic bursts, such as GRB 221009A, the latter scenario can be excluded because the available energy is limited by the magnetars rotational energy to $\sim 2 \times 10^{52}$ erg (Uso 1992; Thompson et al. 2004). The rotational energy, E_{rot} , of an accreting black hole can be extracted via electromagnetic fields, provided there is a strong large-scale magnetic field threading the black hole horizon (Blandford–Znajek mechanism (BZ); Blandford & Znajek 1977). The isotropic equivalent energy of the jet can be written as $E_{\text{jet, iso}} = \eta_j f_b^{-1} E_{\text{rot}}$, where $\eta_j < 1$ is the fraction of rotational energy ending up in the jet, $f_b = 1 - \cos(\theta_j) \approx \theta_j^2/2$ is the beaming factor, θ_j is the jet half-opening angle,

$E_{\text{rot}} = f(a) M_{\text{BH}} c^2$, $f(a_*) = 1 - \sqrt{(1 + \sqrt{1 - a_*^2})/2}$, and a_* is the dimensionless black hole spin. Adopting $\theta_j = 3^\circ.5$ (D’Avanzo et al. 2022)¹² and $\eta_j = 0.5$, we find that a maximally spinning ($a_* = 1$) black hole with $M_{\text{BH}} = 10 M_\odot$ can produce $E_{\text{jet, iso}} \simeq 1.4 \times 10^{57}$ erg, which is comfortably larger than the $E_{\text{kin, ini}}$ required for the “ R_{16} ” scenario. Moderate spins ($a_* \sim 0.5$) would require $M_{\text{BH}} \sim 40 M_\odot$ to meet the model’s energetic requirements. The formation of such massive black holes in the collapsar scenario for long-duration GRBs (with stellar masses $< 40 M_\odot$ in the zero-age main sequence) is not expected (Woosley 1993)—see, however, Siegel et al. (2021) for very massive collapsars. The “ R_{17} ” scenario with baryonic

loading 30 corresponds to $E_{\text{kin, ini}} \geq (3 - 5) \cdot 10^{57}$ erg, which would need $a_* = 1$ and $M_{\text{BH}} \geq 20 M_\odot$. Hence, this scenario is unlikely on energetic grounds. We point out that, although a BZ-powered jet would be initially Poynting-flux-dominated, our internal shock model implies a matter-dominated jet at the dissipation region (see, e.g., Granot et al. 2011; Giannios & Uzdensky 2019; Gottlieb et al. 2022, for possible scenarios for energy conversion in jets). For a non-negligible magnetization at the dissipation radius, a different mechanism for particle energization may instead be invoked, such as magnetic reconnection (e.g., Sironi & Spitkovsky 2014; Guo et al. 2016; Werner et al. 2018).

The energy budget is further typically constrained from the afterglow brightness. Here, it is noteworthy that a part of the energy in the afterglow being dissipated in VHE may relax the requirements on the prompt-phase efficiency, especially for proton-synchrotron models for the VHE emission (Isravel et al. 2022). It should also be noted that a part of the afterglow energy going into thermal particles may equally increase the allowed kinetic energy of the blast wave after the prompt phase. Afterglow observations are also used to infer typical parameters of the GRB. For example, Ren et al. (2022) find a Lorentz factor $\Gamma_0 = 190$ (with room for slightly higher Γ_0 ; see their Figure 3) for the afterglow. This would favor our “ R_{16} ” scenario, which has a typical Lorentz factor $\langle \Gamma_{\text{fin}} \rangle \sim 230$ after the prompt phase.

Our obtained (averaged) maximal proton energies are in the range between 10^{20} and 2×10^{21} eV under the assumption of efficient particle acceleration (see Table 1). Higher proton energies are expected in the SYN-dominated scenarios than the IC-dominated ones, because the acceleration rate is higher due to higher magnetic fields. Our maximal energies are compatible with the values used, e.g., in Das & Razzaque (2022) (100 EeV) to describe the LHAASO VHE photons from EBL interactions. We note that the time delay induced by the extragalactic magnetic fields (EGMFs) requires extremely low field values paired with large proton energies, which means that this challenge can be somewhat mitigated in our SYN-dominated scenario by the high proton energies. We also note that the EGMF-induced delay is very large (assumed to be

¹² This was obtained using a prompt-phase efficiency of 0.2. In our model, this efficiency is lower, which would either necessitate a larger density of the surrounding medium or yield a smaller opening angle.

limited to the observed LHAASO window of 2000s), even under aggressive assumptions for the magnetic field, which means that the protons must be accelerated in the prompt phase of the GRB and further delays induced by the afterglow cannot be accommodated. We find that most of the UHECR protons are emitted within the first 100 s in our model, which is compatible with this picture. Our obtained maximal proton energies are also higher than the maximum corresponding rigidity $R_{\max} \simeq 1\text{--}3$ EV required to describe UHECR data (Heinze et al. 2019)—where details depend on the assumed cutoff shape.

5. Summary and Conclusions

In this letter, we have presented a state-of-the-art multi-messenger emission model for the prompt emission of GRB 221009A. In this model, plasma shells are ejected from a central engine with varying Lorentz factors; these eventually catch up and energy is dissipated in internal shocks. Our radiation model includes the effect of UHECR protons self-consistently, such as the electromagnetic cascade in each shell, generated from secondary electrons, positrons, and photons produced in photohadronic interactions. Our assumptions for the baryonic loading (3 and 30) have been motivated by the paradigm that energetic GRBs, such as GRB 221009A, could be sources of the UHECRs; they are also consistent with the hypothesis that the highest-energy LHAASO photons come from interactions of UHECRs with the EBL.

We have demonstrated that an intermittent engine can reproduce the observed prompt light curves if a quiescent period of about 200 s is included and assuming a variability timescale of ~ 1 s. We have implemented relatively large Lorentz factors and therefore collision radii supported by various arguments (such as $\gamma\gamma$ optical thickness, neutrino nonobservation). Our predicted electromagnetic spectra exhibit spectral indices dominated by synchrotron fast cooling below the MeV peak, except for an ICS-dominated scenario with energy dissipation at high radii that yielded a softer spectral index. Above the peak, ICS can affect the spectral index very strongly, an effect that can extend up to the highest energies and enhance the VHE fluxes. On the other hand, hadronic contributions did not significantly alter the photon spectra. Because pileup effects affect the analysis for nearly all instruments, due to the high brightness of the GRB, the predictive power of our model may be useful. The predicted neutrino emission was consistent with the nonobservation of neutrinos by IceCube due to high predicted peak energies in the range interesting for radio neutrino telescopes. For lower-emission radii (due to variability on shorter timescales and/or lower Lorentz factors) the baryonic loading would likely be constrained to lower values than the ones assumed here. Our findings are consistent with the available rotational energy that can be extracted from a maximally spinning black hole with a mass of the order of $10 M_{\odot}$ if the baryonic loading is not too far away from energy equipartition; our standard assumption of a baryonic loading of 3 is consistent with this picture.

We conclude that GRB 221009A is an interesting object to test the internal shock model and the paradigm that energetic GRBs could be the sources of UHECRs. While direct signatures of cosmic rays (such as neutrinos) have not been seen, the LHAASO observation of TeV photons could point toward UHE proton acceleration. Our model connects the different messengers for the prompt phase of this GRB.

Note. During completion of this work, Liu et al. (2023) appeared. In contrast to their paper, we self-consistently model the photon spectra and account for several emission regions along the jet. Their low(er) emission radii are the consequence of a variability timescale of 82 ms that was derived from an analysis of the GBM light curve up to 219 s, whereas we inferred the variability timescale from the INTEGRAL SPI-ACS light curve also including the bright emission period most relevant for the spectra. Overall, their limits on the baryonic loading are compatible with our findings.

We would like to thank the anonymous referee for a constructive report and intuitive comments. We would like to thank Irene Tamborra, Iftach Sadeh, and Marc Klinger for reading the manuscript and offering useful comments, as well as Sylvia Zhu and Andrew Taylor for discussions around GRB 221009A. A.R. received funding from the Carlsberg Foundation (CF18-0183). M.P. acknowledges support from the MERAC Foundation through the project THRILL and from the Hellenic Foundation for Research and Innovation (H.F.R.I.) under the “Second Call for H.F.R.I. Research Projects to Support Faculty Members and Researchers” through the project UNTRAPHOB (Project ID 3013).

Software: GAMMAPY (Deil et al. 2018; Nigro et al. 2019) and Python v3.9.

ORCID iDs

Annika Rudolph  <https://orcid.org/0000-0003-2040-788X>
 Maria Petropoulou  <https://orcid.org/0000-0001-6640-0179>
 Walter Winter  <https://orcid.org/0000-0001-7062-0289>
 Željka Bošnjak  <https://orcid.org/0000-0001-6536-0320>

References

- Abbasi, R., Ackermann, M., Adams, J., et al. 2021, arXiv:2101.09836
 Abbasi, R., Ackermann, M., Adams, J., et al. 2022, *ApJ*, 939, 116
 Abbott, B. P., Abbott, R., Abbott, T. D., et al. 2017, *PhRvL*, 119, 161101
 Ai, S., & Gao, H. 2022, arXiv:2210.14116
 Alves Batista, R. 2022, arXiv:2210.12855
 Blandford, R. D., & Znajek, R. L. 1977, *MNRAS*, 179, 433
 Bustamante, M., Heinze, J., Murase, K., & Winter, W. 2017, *ApJ*, 837, 33
 Chiang, J., & Dermer, C. D. 1999, *ApJ*, 512, 699
 Crumley, P., Caprioli, D., Markoff, S., & Spitkovsky, A. 2019, *MNRAS*, 485, 5105
 Daigne, F., Bosnjak, Z., & Dubus, G. 2011, *A&A*, 526, A110
 Daigne, F., & Mochkovitch, R. 1998, *MNRAS*, 296, 275
 Das, S., & Razzaque, S. 2022, arXiv:2210.13349
 D’Avanzo, P., Ferro, M., Brivio, R., et al. 2022, *GCN*, 32755, 1
 de Ugarte Postigo, A., Izzo, L., Pugliese, G., et al. 2022, *GCN*, 32648, 1
 Deil, C., et al. 2018, *ICRC (Busan)*, 35, 766
 Dichiaro, S., Gropp, J. D., Kennea, J. A., et al. 2022, *ATel*, 15650, 1
 Dominguez, A., Primack, J. R., Rosario, D. J., et al. 2011, *MNRAS*, 410, 2556
 Frederiks, D., Lysenko, A., Ridnaia, A., et al. 2022, *GCN*, 32668, 1
 Gao, S., Kashiyama, K., & Mészáros, P. 2013, *ApJL*, 772, L4
 Gao, S., Pohl, M., & Winter, W. 2017, *ApJ*, 843, 109
 Ghirlanda, G., Nappo, F., Ghisellini, G., et al. 2018, *A&A*, 609, A112
 Giannios, D., & Uzdensky, D. A. 2019, *MNRAS*, 484, 1378
 Gottlieb, O., Liska, M., Tchekhovskoy, A., et al. 2022, *ApJL*, 933, L9
 Granot, J., Komissarov, S. S., & Spitkovsky, A. 2011, *MNRAS*, 411, 1323
 Guo, F., Li, X., Li, H., et al. 2016, *ApJL*, 818, L9
 Heinze, J., Fedynitch, A., Boncioli, D., & Winter, W. 2019, *ApJ*, 873, 88
 Huang, Y., Hu, S., Chen, S., et al. 2022, *GCN*, 32677, 1
 Hummer, S., Baerwald, P., & Winter, W. 2012, *PhRvL*, 108, 231101
 Isravel, H., Pe’er, A., & Begue, D. 2022, arXiv:2210.02363
 Kimura, S. S. 2022, arXiv:2202.06480
 Kobayashi, S., Piran, T., & Sari, R. 1997, *ApJ*, 490, 92
 Kumar, P., & Zhang, B. 2015, *PhR*, 561, 1
 Lesage, S., Veres, P., Roberts, O.J., et al. 2022, *GCN*, 32642, 1

- Liu, R.-Y., Zhang, H.-M., & Wang, X.-Y. 2023, *ApJL*, 843, 7
- Mirabal, N. 2022, *MNRAS*, 519, L85
- Murase, K., Mukhopadhyay, M., Kheirandish, A., Kimura, S. S., & Fang, K. 2022, *ApJL*, 941, L6
- Nigro, C., Deil, C., Zanin, R., et al. 2019, *A&A*, 625, A10
- Omodei, N., Bruel, P., Bregeon, J., et al. 2022, GCN, 32916, 1
- Pillera, R., Bissaldi, E., Omodei, N., et al. 2022, GCN, 32658, 1
- Rees, M. J., & Meszaros, P. 1992, *MNRAS*, 258, 41P
- Ren, J., Wang, Y., & Zhang, L.-L. 2022, arXiv:2210.10673
- Rudolph, A., Petropoulou, M., Bošnjak, v., & Winter, W. 2022, arXiv:2212.00765
- Siegel, D. M., Agarwal, A., Barnes, J., et al. 2021, *ApJ*, 941, 28
- Sironi, L., & Spitkovsky, A. 2014, *ApJL*, 783, L21
- The IceCube Collaboration 2022, GCN, 32665, 1
- Thompson, T. A., Chang, P., & Quataert, E. 2004, *ApJ*, 611, 380
- Uso, V. V. 1992, *Natur*, 357, 472
- Ursi, A., Panebianco, G., Pittori, C., et al. 2022, GCN, 32650, 1
- Veres, P., Burns, E., Bissaldi, E., et al. 2022, GCN, 32636, 1
- Vietri, M. 1995, *ApJ*, 453, 883
- Waxman, E. 1995, *PhRvL*, 75, 386
- Werner, G. R., Uzdensky, D. A., Begelman, M. C., Cerutti, B., & Nalewajko, K. 2018, *MNRAS*, 473, 4840
- Woosley, S. E. 1993, *ApJ*, 405, 273
- Zhang, B. T., Murase, K., Ioka, K., et al. 2022, arXiv:2211.05754